PKIKPPKIKP Versus *PKiKPPKiKP*: A New Pair of Seismic Phases for Mapping the Earth's Inner Core

Marian Ivan[1], Laura Petrescu[*1,2], Xiaobo He[3], and Rongjiang Wang[4]

Abstract

The Earth's uppermost inner core (IC) is a critical boundary region where thermal, compositional, and mechanical interactions between the liquid outer-core and solid IC influence solidification processes and the geodynamo. Previous studies relied primarily on *PKIKP–PKiKP* seismic phases recorded at epicentral distances of 130°–142°. Here, we introduce a complementary approach by analyzing *PKIKPPKIKP–PKiKPPKiKP* differential times near 90° from deep earthquakes. These rare, multiply reflected phase pairs sample the IC on both descending and ascending paths and share similar trajectories, minimizing the influence of mantle heterogeneity. We measure their differential arrival times via waveform cross correlation in the 0.7–2 Hz frequency band and compute residuals with respect to synthetic seismograms that account for earthquake source mechanisms. These residuals are directly sensitive to *P*-wave velocity anomalies in the IC. In addition, we identify a new small set of *PKIKPPKIKP* and *PKPbcPKPbc* arrivals near 60°, which could support future studies of deeper IC regions. Statistical analysis using Akaike and Bayesian information criteria favors a single-parameter isotropic model, suggesting that the observed residuals can be explained without introducing additional anisotropy. Our results highlight the untapped value of rare, multiply reflected core phase pairs in probing Earth's deep interior.

Cite this article as Ivan, M., L. Petrescu, X. He, and R. Wang (2026). *PKIKPPKIKP* Versus *PKiKPPKiKP*: A New Pair of Seismic Phases for Mapping the Earth's Inner Core, *Seismol. Res. Lett.* **XX**, 1–14, doi: 10.1785/0220260014.

Supplemental Material

Introduction

The Earth's solid inner core (IC) plays a critical role in planetary evolution, contributing to the geodynamo and core–mantle dynamics through thermal and compositional processes (Alboussière *et al.*, 2010; Deguen, 2012; Landeau *et al.*, 2017). Seismic studies have long suggested that the IC exhibits complex, large-scale heterogeneity (Tanaka and Hamaguchi, 1997; Niu and Wen, 2001; Stroujkova and Cormier, 2004; Irving and Deuss, 2011), with variations in *P*-wave velocity potentially linked to solidification processes, thermal history, and core–mantle coupling (Aubert *et al.*, 2008; Monnereau *et al.*, 2010; Gubbins *et al.*, 2011; Deguen *et al.*, 2013; Tkalčić *et al.*, 2024). Traditionally, constraints on the IC's velocity structure have come primarily from the analysis of differential travel times between specific seismic phases that have similar propagation trajectories through or near the IC boundary, such as *PKIKP*, *PKiKP*, or *PKPbc* (Tkalčić, 2015). Although PKIKP rays have been essential in identifying velocity patterns in the IC, their paths are predominantly limited to quasi-equatorial directions, meaning they travel nearly perpendicular to Earth's spin axis which leads to a strong sampling bias, with fewer polar measurements identified only for *PKIKP* (Brett and Deuss, 2020). As a result, there is a lack of quasi-polar ray paths needed to probe anisotropy along the rotation axis. In addition, despite the global expansion of seismic networks, significant regional gaps remain in the sampling of the IC, particularly beneath regions such as South America, the Central and South Atlantic, parts of the Pacific Ocean, North Africa, and Europe. These limitations result in incomplete coverage and hinder our ability to fully resolve the IC's heterogeneous structure.

Here, we propose a framework for reliably and systematically detecting other core-propagating seismic phases, such as *PKIKPPKIKP* (also denoted *PKPdfPKPdf*), which is paired with either *PKiKPPKiKP* at epicentral distances of approximately 80° to 98° or *PKPbcPKPbc* at approximately 50° to 65°. *PKIKPPKIKP* propagates through the uppermost IC, reflects off the Earth surface, and bounces back, propagating again through the IC on the other side, essentially sampling opposite sides of the Earth. *PKiKPPKiKP* follows a very similar

1. University of Bucharest, Bucharest, Romania, https://orcid.org/0000-0001-5462-4546 (LP); 2. National Institute for Earth Physics, Măgurele, Romania; 3. Marine Science and Technology College, Zhejiang Ocean University, Zhoushan, China, https://orcid.org/0000-0002-6357-8948 (XH); 4. GFZ Helmholtz Centre for Geosciences, Potsdam, Germany

*Corresponding author: laura.petrescu@infp.ro

© Seismological Society of America

Downloaded from pubs.geoscienceworld.org/ssa/srl/article-pdf/doi/10.1785/0220260014/8427141/srl-2026014.1.pdf by Southern University of Science and Technology of China user on 28 October 2026

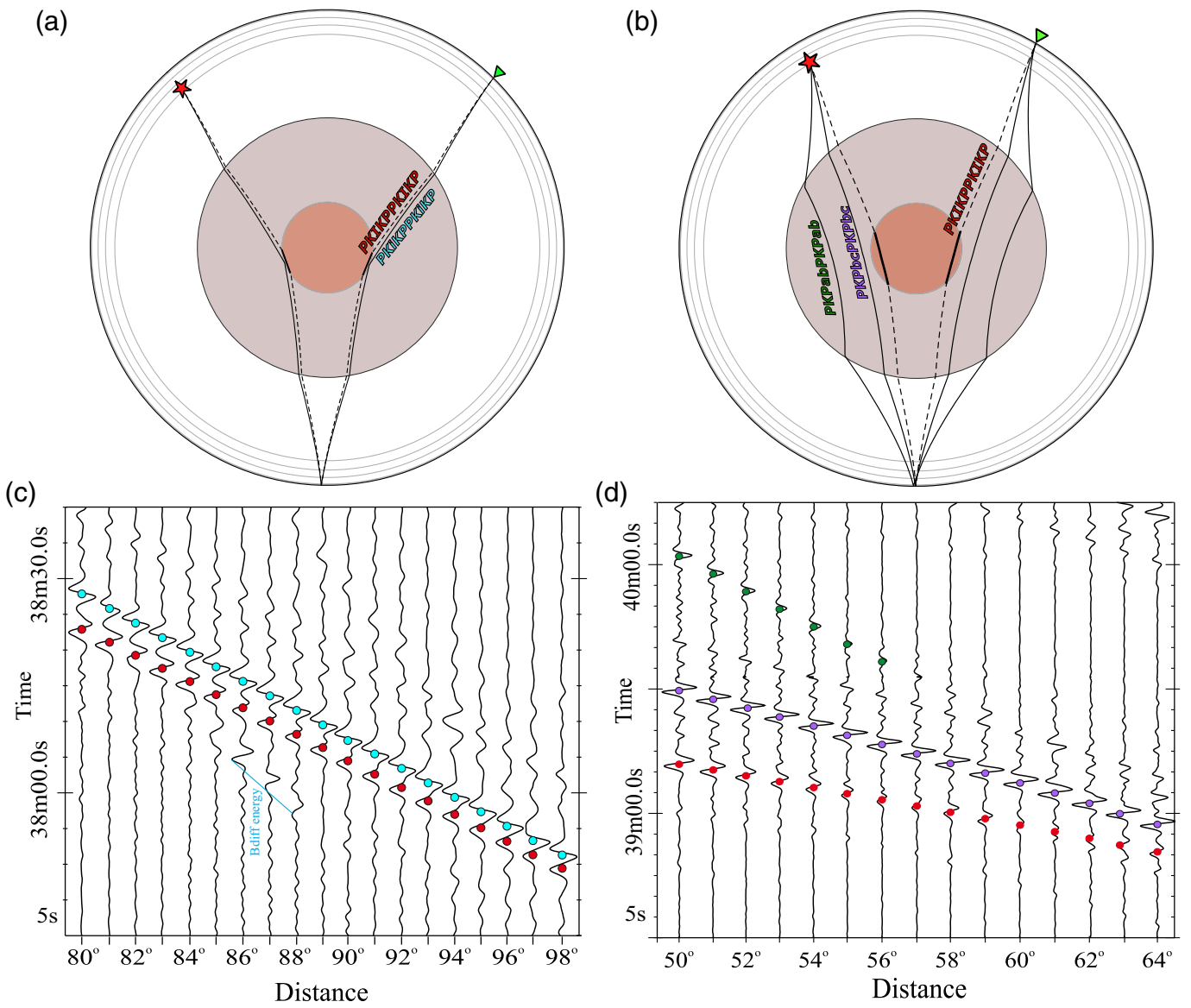

Figure 1. Predicted ray paths and broadband synthetics for selected inner-core (IC) phases. Synthetics are computed using the QSSP code for a vertical-component source at 300 km depth. (a) Double leg ray paths for a station at 90°, whereas a station at ~135° records single leg *PKIKP* and *PKiKP*. (b) Double leg ray paths for a station at 60°, whereas a station at ~150° records all three phases single leg *PKPdf*, *PKPbc*, and *PKPab*. (c) Synthetic waveforms for epicentral distances between 80° and 98° showing arrivals of *PKIKPPKIKP* (red dots) and *PKiKPPKiKP* (blue dots). Note the similarity to the arrival times of IC phases modeled with QSSP with those predicted from TauP code based on the AK135 model (colored dots). (d) Synthetic waveforms for distances between 50° and 64° highlighting *PKIKPKIKP* (red dots), *PKPbcPKPbc* (blue dots), and *PKPabPKPab* (green dots). The color version of this figure is available only in the electronic edition.

trajectory but reflects off the IC-outer-core boundary (Fig. 1a). Differences between these two phases can thus be attributed to structural heterogeneities in the uppermost IC of the Earth. Similarly, *PKPbcPKPbc* propagates through the outer core, near the IC boundary (Fig. 1b), although the larger separation from *PKIKPPKIKP* may require mantle corrections.

Although certain branches, such as *PKPbcPKPbc*, are occasionally reported in seismic bulletins (e.g., by the International Seismological Centre [ISC]; Lentas *et al.*, 2019); others, including *PKIKPPKIKP* and *PKPabPKPab*, are rarely analyzed (Bréger, Romanowicz, *et al.*, 2000; Rost and Garnero, 2004; Frost and Romanowicz, 2017; Phạm and Tkalčić, 2023). Our work shows that both these phases and especially *PKiKPPKiKP*, can be reliably identified in seismic recordings more frequently than previously recognized, using only deep earthquakes, with simple-source, downward-radiating focal mechanisms, and matched 1 Hz synthetics. These phase pairs offer an excellent opportunity to tap into underutilized information about the IC.

To fully exploit the potential of these exotic phases, we extract their relative travel-time delays using full-waveform synthetic seismograms (Fig. 1c,d) and cross-correlation techniques.

Downloaded from pubs.geoscienceworld.org/ssa/srl/article-pdf/doi/10.1785/0220260014/8427141/srl-2026014.1.pdf by Southern University of Science and Technology of China user on 28 October 2026

These time delays can then be incorporated into data sets of conventional phase pairs (Waszek and Deuss, 2011; Ivan *et al.*, 2018; Frost *et al.*, 2021) to construct seismic tomography models of the IC (Ivan *et al.*, 2018; Burdick *et al.*, 2019). Despite being fewer in number, their sampling geometry and combined contribution can help reduce equatorial bias, fill critical coverage gaps in some areas, and introduce directional sensitivity that complements traditional data sets, providing information beneath some IC regions historically undersampled by global networks and *PKIKP* versus *PKiKP* data sets.

Data and Methods

Criteria for detection of multipath IC phases

To guarantee sufficient signal-to-noise ratio (SNR) for the often-elusive multileg *PKiKPPKiKP–PKIKPPKIKP* phases, events from the ISC catalog between 1995 and 2024 were selected based on the following criteria:

1. magnitudes $M_w \geq 6.0$ to ensure adequate source energy;
2. intermediate or deep focal depths to reduce crustal and uppermost mantle scattering;
3. focal mechanisms characterized by high-angle dip-slip faulting (conjugate planes dipping near 45° and rake near 90°, Fig. 2) to maximize downward vertical *P*-wave radiation. For such events, we expect no significant differences in relative amplitudes evaluated with slightly different focal mechanisms as provided by various agencies;
4. rejection of compound or closely spaced ruptures of similar magnitudes, which can produce pulses or complex wavefields that might mimic the *PKiKPPKiKP* or *PKPbcPKPbc* phases; and
5. clarity and simplicity of the single-leg *PKIKP* and subsequent *PKP* arrivals. If these phases exhibit complex waveforms or low SNR, it is unlikely that their double-leg counterparts (e.g., *PKIKPPKIKP*) produce visible or interpretable energy. Therefore, we retained only those events with stations showing simple, high-SNR *PKP* waveforms, free from interference or secondary arrivals that could obscure later phases (Fig. S1, available in the supplemental material to this article).

We manually screened such events for waveform quality using broadband stations with high SNR (greater than 3) across the global networks (Fig. 2).

From these earthquakes, we compiled an initial data set of *PKP* phases to evaluate phase visibility and waveform quality before searching for the multileg branches. The ISC bulletin was used as a primary reference to identify events and stations where core phases had been previously reported (as either P′P ′, *PKPPKP* or similar), providing an initial guide for data selection. However, not all usable observations were listed in the ISC catalog, and additional recordings showing clear *PKP* arrivals (based on the updated Ivan *et al.*, 2018 data set) were included following manual inspection. This selection ensured that any detected *PKiKPPKiKP–PKIKPPKIKP* energy could be confidently attributed to genuine IC reflections, rather than to unmodeled complexities in the classical *PKP* phases.

To provide a theoretical basis for phase identification, we computed full-waveform synthetic seismograms using the Synthetic Seismograms for a Spherical Earth (QSSP) code (Wang *et al.*, 2017), a hybrid method that models seismic-wave propagation through a spherically symmetric, self-gravitating Earth including the atmosphere, ocean, mantle, liquid outer core, and solid IC. This approach combines numerical and analytical techniques to capture the full-frequency spectrum, accounting for effects such as gravity coupling, static offsets, and multiple reflections. Simulations were performed using the AK135 global velocity model (Kennett *et al.*, 1995) and full moment tensor source parameters from the Global Centroid Moment Tensor (Global CMT) catalog (Dziewonski *et al.*, 1981; Ekström *et al.*, 2012), ensuring physically consistent and realistic earthquake radiation patterns. We focused on the epicentral distance range of 80°–100°, where the *PKIKPPKIKP–PKiKPPKiKP* phase pair is most clearly separated in time and amplitude.

Phase identification for *PKIKPPKIKP* and their reference counterparts was performed through a systematic, joint inspection of observed and synthetic broadband seismograms, primarily on the vertical component, with the radial component also examined where available (Fig. 3). Candidate arrivals were first located using theoretical travel times from 1D models and then verified by comparing observed seismograms with synthetic waveforms to confirm coherent core-phase energy above the numerical noise level. To suppress long-period noise and enhance phase coherence, both data sets were filtered with a zero-phase Butterworth band-pass filter in the range 0.7–2 Hz, consistent with the frequency band routinely used for *PKIKP–PKiKP* studies (Cao and Romanowicz, 2004). In the 80°–100° distance range, *PKIKPPKIKP* recordings, like *PKIKP* around 135°, can exhibit precursor energy generated by diffraction near the B caustic (~70° for the double-leg ray). Previous studies have shown that appropriate band-pass filtering can reduce the contribution of long-period precursor energy and improve identification of the target arrivals (Cao and Romanowicz, 2004; Ivan and He, 2017). A large-amplitude *PKPbc* underside reflection from the Moho could, in principle, generate a precursor that arrives nearly simultaneously with *PKIKPPKIKP*, making identification ambiguous at a single station. To evaluate this possibility for the specific case considered here, we computed synthetics at virtual stations surrounding the receiver and performed a slowness analysis (Fig. S2). Only events showing consistent behavior in both data and synthetics were retained for differential-time analysis. High-SNR recordings of double legs *PKIKPPKIKP* around 60° are shown in Figure 4.

Delay time measurement procedure

Assuming that each phase pair shares nearly identical mantle and outer-core paths, any residual between observed and

Downloaded from pubs.geoscienceworld.org/ssa/srl/article-pdf/doi/10.1785/0220260014/8427141/srl-2026014.1.pdf by Southern University of Science and Technology of China user on 28 October 2026

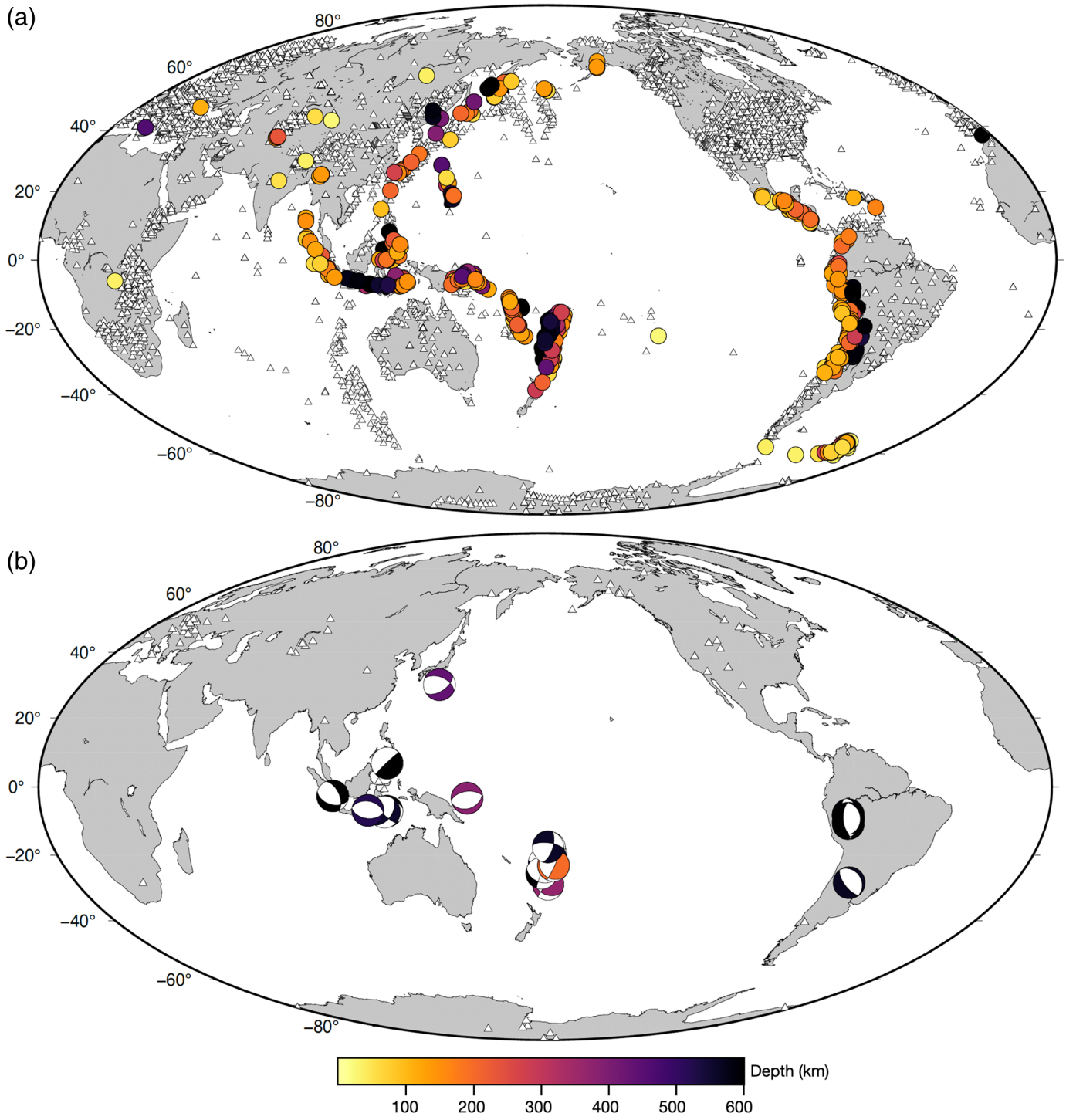

synthetic differential times primarily reflects *P*-wave velocity perturbations along the IC segments traversed by the descending and ascending legs of *PKIKPPKIKP*. To quantify the timing differences sensitive to IC structure, we measured the differential arrival times between *PKIKPPKIKP* and their corresponding reference phases (*PKiKPPKiKP* or *PKPbcPKPbc*), with respect to synthetic travel times (Tables S1 and S2). Importantly, these measurements do not rely on aligning observed and synthetic waveforms in absolute time; instead, the time separation between the phase pairs is determined

Figure 2. (a) Global map of earthquakes (circles colored as a function of depth) and seismic stations (white triangles) for which *PKIKP–PKiKP* phase pairs were clearly detected (updated from Ivan *et al.*, 2018), used for a subsequent search of multileg *PKIKPPKIKP–PKPbcPKPbc* or *PKiKPPKiKP* phases. (b) Global map of earthquakes (focal mechanisms colored as a function of depth) and seismic stations for which these multileg phase pairs were successfully detected and further analyzed. The color version of this figure is available only in the electronic edition.

Downloaded from pubs.geoscienceworld.org/ssa/srl/article-pdf/doi/10.1785/0220260014/8427141/srl-2026014.1.pdf by Southern University of Science and Technology of China user on 28 October 2026

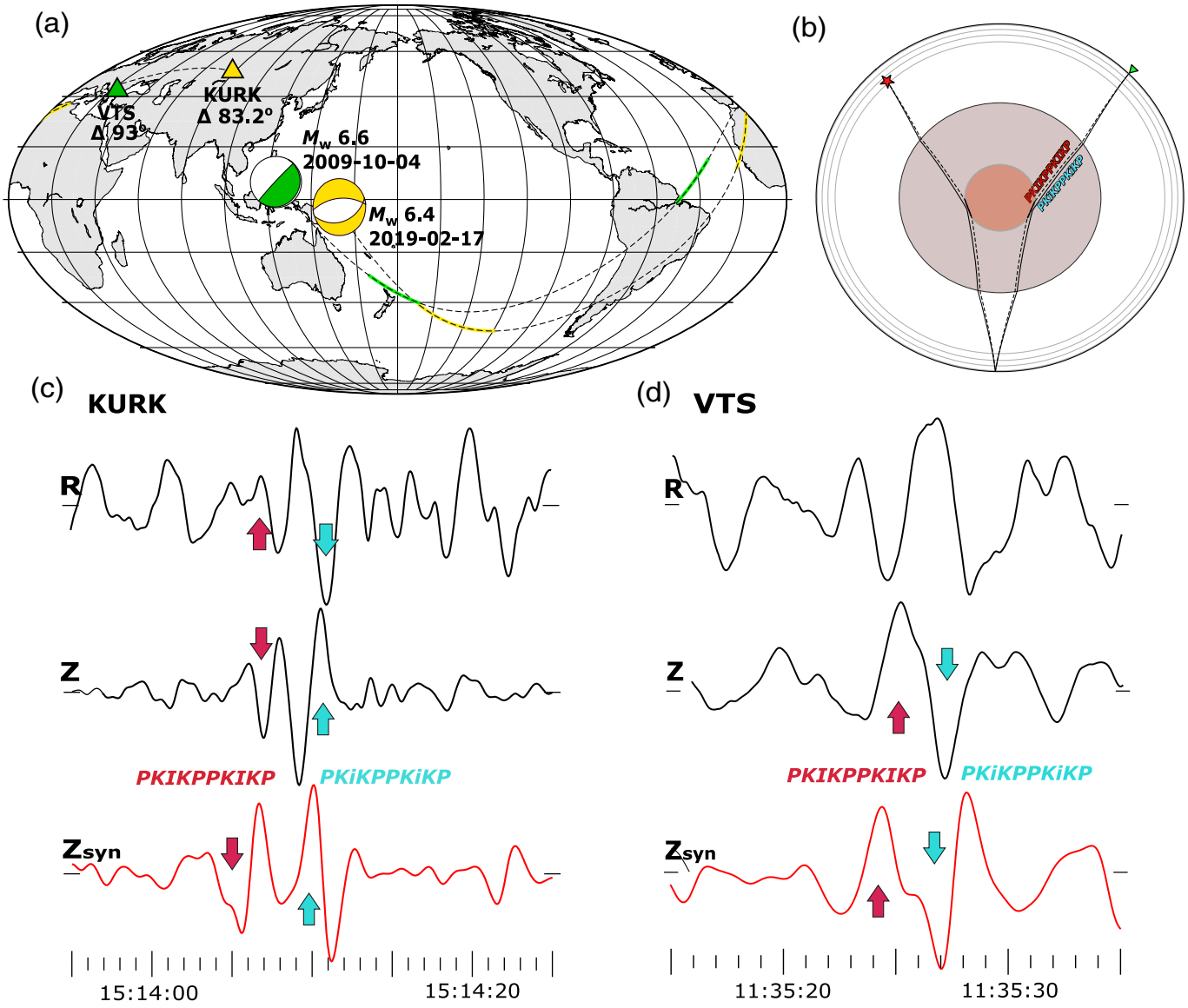

Figure 3. Broadband observed and synthetic seismograms for selected events and stations. (a) Global map of earthquake focal mechanisms, recording seismic stations (triangles), and *PKIKPPKIKP* paths throughout the Earth (dashed line) and through the IC (thick colored line). (b) Theoretical ray paths for the *PKIKPPKIKP* and the *PKiKPPKiKP* rays through an ideal Earth from an earthquake (red star) recorded at a seismic station 90° away. (c) KURK station recording of the 17 February 2019 New Ireland event (radial and vertical components, top; synthetic vertical, bottom). The Global Centroid Moment Tensor (Global CMT) solution indicates negative polarity for *PKIKPPKIKP* and positive for *PKiKPPKiKP*. Arrows mark predicted arrival times. (d) VTS station recording of the 4 October 2009 Mindanao event. Time is in UT (Universal Time). The color version of this figure is available only in the electronic edition.

independently for observations and synthetics. Because both phase pairs traverse mantle and outer-core heterogeneities, the difference between their absolute travel times and those predicted by 1D models will always be slightly different. However, we are interested in how the time difference between these pairs differs from the time difference predicted by 1D model synthetics, which is the part sensitive to IC velocity structure. In this formulation, absolute arrival times are not required, as they are strongly affected by mantle structure, whereas the differential times between phase pairs largely cancel these effects. Thus, this differential travel time is

$$\Delta T = (T_{\mathrm{REF}} - T_{\mathrm{core}})_{\mathrm{obs}} - (T_{\mathrm{REF}} - T_{\mathrm{core}})_{\mathrm{syn}}, \quad (1)$$

in which REF denotes either *PKiKPPKiKP* or *PKPbcPKPbc*, and core denotes *PKIKPPKIKP*. Conceptually, this residual time difference can be expressed as the cumulative effect of small velocity deviations $\delta v/v$ integrated along both IC paths,

Downloaded from pubs.geoscienceworld.org/ssa/srl/article-pdf/doi/10.1785/0220260014/8427141/srl-2026014.1.pdf by Southern University of Science and Technology of China user on 28 October 2026

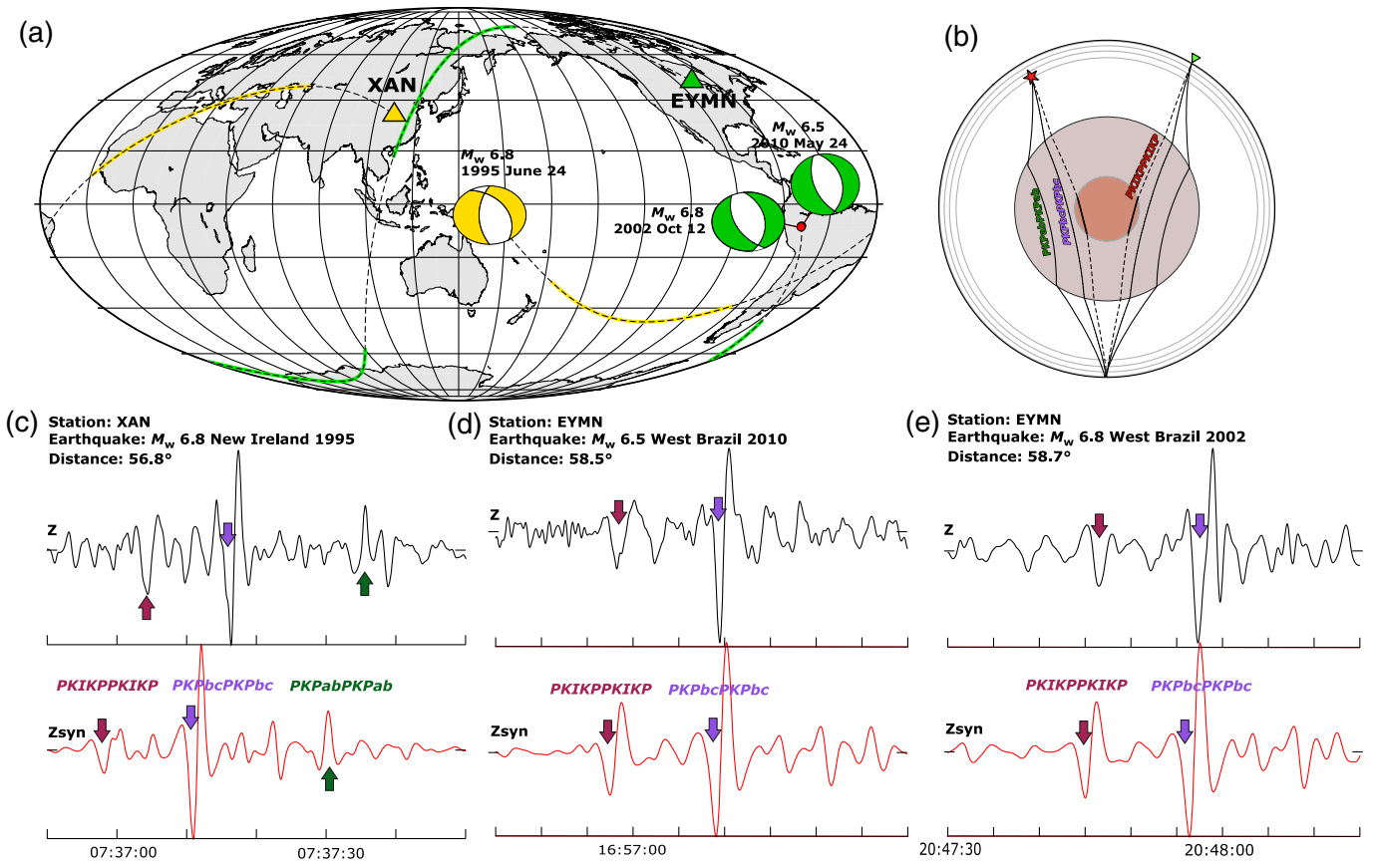

Figure 4. Examples of high-quality broadband seismograms for selected events at different stations. (a) Global map of earthquake focal mechanisms, recording seismic stations (colored triangles), and *PKIKPPKIKP* paths throughout the Earth (dashed line) and through the IC (thick line). (b) Theoretical ray paths for the *PKIKPPKIKP* and the *PKPbcPKPbc* and *PKPabPKPab* rays through an ideal Earth from an earthquake (red star) recorded at a seismic station 58° away. (c) XAN station recording of the 24 June 1995 New Ireland event, showing all *PKPPKP* branches. (d) EYMN station recording of the 24 May 2010 West Brazil event. (e) EYMN station recording of the 12 October 2002 West Brazil event. Time is in UT. The color version of this figure is available only in the electronic edition.

illustrating the potential sensitivity of these new phases to localized heterogeneity at depth:

$$\Delta T \approx \int_{\text{desc}} \frac{\delta v}{v} \mathrm{d}t + \int_{\text{asc}} \frac{\delta v}{v} \mathrm{d}t, \tag{2}$$

in which dt is the propagation time element in the reference model. The integral is performed over the two IC paths of *PKIKPPKIKP* (descending and ascending legs, respectively). Thus, each measurement is linked to variations in *P*-wave velocity along their multilegged trajectories through the IC.

Once confidently identified, differential arrival times between *PKIKPPKIKP* and the reference phases (*PKiKPPKiKP* or *PKPbcPKPbc*) were measured via cross correlation. Windows of approximately 0.5 s were defined for both the reference and target phases. Cross correlation involves sliding one window over the other and computing the product at each lag, yielding a function $C(\tau)$ whose extrema indicate optimal alignment between the two phase windows. Note that *PKIKPPKIKP* and *PKiKPPKiKP* exhibit opposite polarities. *PKIKPPKIKP* and *PKPbcPKPbc* show the same polarity.

The resulting lag between the two windows is used to compute the observed differential time Δt_{obs}. The same procedure is applied to the corresponding synthetic seismograms to obtain Δt_{syn}, ensuring consistency in processing. The difference, $\Delta t_{\text{obs}} - \Delta t_{\text{syn}}$, represents the IC-sensitive travel-time residual. This approach provides a robust measure of the relative timing between phases without requiring identification of an absolute arrival time, which is particularly important in the presence of nearby noise and waveform complexity. Unlike approaches that rely on manually aligned or picked phase arrivals and comparisons with predictions from a reference model (e.g., Young *et al.*, 2013; Lythgoe *et al.*, 2014; Frost and Romanowicz, 2017; Brett and Deuss, 2020), our methodology avoids absolute-time picking altogether. Instead, we compute full-waveform synthetics for each event based on its moment tensor solution and determine phase separations through cross correlation applied consistently to both observed and synthetic data. This explicit incorporation of source radiation patterns, polarity, and waveform complexity is essential

Downloaded from pubs.geoscienceworld.org/ssa/srl/article-pdf/doi/10.1785/0220260014/8427141/srl-2026014.1.pdf by Southern University of Science and Technology of China user on 28 October 2026

for isolating and reliably measuring these weak multileg phases, for which manual picking of absolute arrivals is often ambiguous or unstable.

To estimate the uncertainty of the measured time differences, several sources of error must be considered, including propagation effects, finite signal bandwidth, intrinsic waveform resolution, and reference model limitations. An empirical proxy for this uncertainty is the observed scatter in differential times from collocated or nearby sampling geometries, which reflects a combination of measurement uncertainty and small-scale structural variability (Frost and Romanowicz, 2017). Using *PKiKP–PKIKP* differential times from station clusters sampling a limited IC region, Ivan *et al.* (2018) report variability on the order of ~0.3 s. In this study, we instead derive a physically motivated estimate of the timing uncertainty based on signal theory, using a Cramér–Rao type formulation (Kay, 1993) that relates uncertainty to the SNR and the frequency content of the waveform. The resulting uncertainties are reported as $\pm 2\sigma$. Although such estimates are not routinely provided in classical studies of phase differences, they offer a consistent lower-bound constraint on timing precision. Full details of the formulation and a summary of the resulting uncertainties are provided in the supplemental material.

Statistical testing of anisotropy

To assess whether the differential travel-time residuals show a statistically significant dependence on ray direction through the IC, we performed model selection using the Akaike Information Criterion (AIC, Akaike, 1973) and Bayesian Information Criterion (BIC, Schwarz, 1978). Angular dependence of IC travel times has been widely used to investigate IC anisotropy (Tanaka and Hamaguchi, 1997; Frost and Romanowicz, 2017; Burdick *et al.*, 2019; Brett and Deuss, 2020). We compared three alternative formulations in terms of the angles ζ_a and ζ_d, defined as the angles between the ascending and descending IC ray segments, respectively, and Earth's rotation axis: (1) a pure isotropic model, in which the differential travel-time residual is independent of ζ_a and ζ_d; (2) a linear angular model in $(\cos^2\zeta_d + \cos^2\zeta_a)/2$; and (3) a parabolic model, which includes $(\cos^4\zeta_d + \cos^4\zeta_a)/2$. For each formulation, we determined the best-fitting parameters and calculated the corresponding AIC and BIC values. Lower AIC and BIC values indicate stronger support for a model after accounting for its number of free parameters, assessing whether introducing angular dependence provides a statistically meaningful improvement over the isotropic model and whether the data favor a linear or nonlinear dependence.

Results

A systematic search of global broadband data revealed clear recordings of the multiply reflected *PKIKPPKIKP* and *PKiKPPKiKP* phases from several deep-focus earthquakes between 1995 and 2023. These phases were identified at epicentral distances of 80°–100°, in excellent agreement with full-waveform synthetic predictions computed using the AK135 reference model and QSSP simulations and arrival times evaluated with TauP toolkit (Crotwell *et al.*, 1999). The resulting data set is characterized by SNR ranging between 1.2 and 9.4 with a mean SNR of 3.4. Earthquake source half-duration values range from 0.6 to 4.7 s, with a median of 1.0 s and a mean of 1.31 s, indicating predominantly short-duration source time functions with only a small number of moderately extended ruptures. We note that, although the ISC Bulletin typically reports *PKPPKP* arrivals only for large, deep events ($M_w \geq 6.8$), our observations demonstrate that these phases can also be detected in smaller events ($M_w \approx 6.0$) when recorded under favorable conditions.

At shorter epicentral distances (50°–65°), distinct arrivals corresponding to *PKIKPPKIKP* and *PKPbcPKPbc* are also observed (Fig. 4), consistent with synthetic predictions for the same geometry (Fig. S3). In several high-quality recordings, the additional branch AB is recognizable, confirming its viability as observational constraints in IC studies (Bréger, Romanowicz, *et al.*, 2000; Frost and Romanowicz, 2017). This improved detectability is not solely due to favorable signal-to-noise conditions but also reflects careful selection of events characterized by simple source time functions and strong downward energy radiation—features that enhance coherence and minimize phase interference. Moreover, the distribution of ζ angles for the *PKIKPPKIKP* branches (Fig. S3) confirms that, although most trajectories are equatorial ($\zeta \geq 35°$), the data set also contains polar ($\zeta < 35°$) and ultra-polar ($\zeta < 20°$) trajectories. These polar branches provide complementary directional sampling relative to the predominantly equatorial coverage of conventional *PKP* phases.

All earthquakes for which we successfully identified the *PKPPKP* phase in Table S1 also yielded clear observations of *PKIKP* versus *PKiKP* or *PKIKP* versus *PKPbc* (Fig. S1), with differential times that are consistent with previous studies. This consistency supports the reliability of our *PKIKPPKIKP* measurements and effectively rules out the possibility of complex source effects compromising the results, given that reliable *PKIKP* and *PKiKP* arrivals were also recorded. For events lacking clear *PKP* signals, we did not pursue further *PKPPKP* identification. Frequently, high amplitudes of *PKKPbc* in the same events often coincide with detectable *PKIKPPKIKP* energy, especially when *PKIKP–PKiKP* differential times (130°–142° range) align with expected values for events with simple rupture characteristics.

To further evaluate the consistency of the identified multilegged phases with their predicted travel-time behavior, we performed a slowness-time array analysis using the 25 European stations that recorded the 25 July 2004 Southern Sumatra earthquake (Fig. 5). The resulting vespagram and beam stack show coherent energy close to the predicted slownesses and arrival times of *PKIKPPKIKP* and *PKiKPPKiKP*. Linear regressions

Downloaded from pubs.geoscienceworld.org/ssa/srl/article-pdf/doi/10.1785/0220260014/8427141/srl-2026014.1.pdf by Southern University of Science and Technology of China user on 28 October 2026

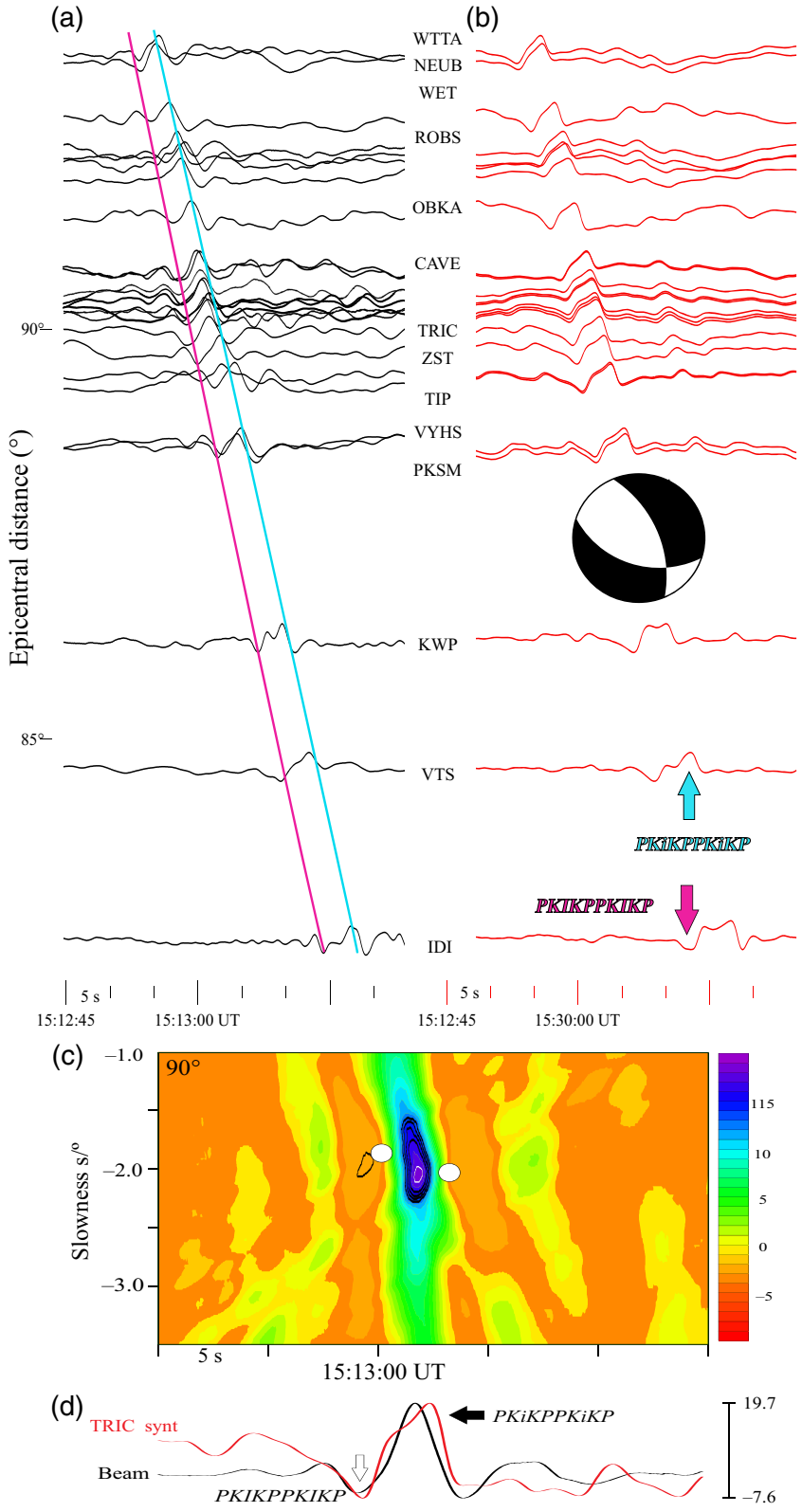

Figure 5. Detection and array analysis of the *PKIKPPKIKP* and *PKiKPPKiKP* phases for the 25 July 2004 Southern Sumatra earthquake. (a) Vertical-component broadband recordings and (b) corresponding synthetics, with the fitted moveout of the *PKIKPPKIKP* and *PKiKPPKiKP* arrivals indicated. The inset shows the focal mechanism of the 2004 Sumatra earthquake. (c) Slowness-time vespagram showing coherent energy near the expected slowness (white circles). (d) Array stack compared with the synthetic prediction at station TRIC, showing coherent enhancement at the *PKiKPPKiKP* arrival. The color version of this figure is available only in the electronic edition.

of the observed arrival times as a function of epicentral distance yield slopes of −1.91 ± 0.05 s/deg for *PKIKPPKIKP* and −2.07 ± 0.05 s/deg for *PKiKPPKiKP*, with $R^2 > 0.98$ in both cases. The agreement between the predicted and observed slowness, together with the high-correlation coefficients of the moveout fits, provides an independent consistency check on the identification of these multilegged phases.

Further, we extracted differential travel times between the multiply reflected *PKIKPPKIKP* phase and the reference phases (*PKiKPPKiKP* or *PKPbcPKPbc*) by cross correlating each phase pair within the observed data set, and separately within the synthetic seismograms. We then calculated the residual differential travel times as the differences between the observed and synthetic measurements (Tables S1 and S2). These residuals ($\Delta t_{obs} - \Delta t_{syn}$) are directly sensitive to seismic velocity anomalies in the uppermost IC. Because the *PKIKPPKIKP–PKiKPPKiKP* residuals represent cumulative travel-time perturbations along both IC legs, separating the contribution of each leg is inherently nonunique at the measurement level. Previous work (Bréger, Romanowicz, *et al.*, 2000; Rost and Garnero, 2004) noted a similar difficulty for the double-leg *P′P′df*phase and emphasized the importance of using independent single-leg observations to constrain each path segment.

The ray-path geometry nevertheless provides qualitative insight. In several cases, portions of the multileg paths overlap regions previously

Downloaded from pubs.geoscienceworld.org/ssa/srl/article-pdf/doi/10.1785/0220260014/8427141/srl-2026014.1.pdf by Southern University of Science and Technology of China user on 28 October 2026

sampled by conventional *PKiKP–PKIKP* observations. This overlap allows a first-order comparison with existing single-leg constraints, suggesting how different segments of the path may contribute to the total delay time. Where both legs intersect previously sampled regions, the combined behavior is broadly consistent with the cumulative residuals observed here. A full quantitative separation of contributions from individual legs requires joint inversion of single- and multileg data sets, which is beyond the scope of the present study.

The newly identified multileg *PKIKPPKIKP* phases, colored by their interpreted differential delay times with *PKiKPPKiKP* or *PKPbcPKPbc*, along with the updated data set of conventional *PKIKP–PKiKP* ray paths are presented in Figure 6. The spatial distribution reveals a consistent correspondence between the exotic and conventional measurements, further supporting the reliability of the new observations. This agreement across independent data sets demonstrates that the measured time differences are physically meaningful and that the dual-leg phases provide coherent, complementary sampling of the upper IC alongside their single-leg counterparts.

Several representative cases highlight how observed *PKIKPPKIKP–PKiKPPKiKP* differential times can be interpreted through their constituent ray paths. The 29 March 1998 event recorded at PLCA shows a differential time of −0.05 s. Its descending leg samples the IC beneath southern Japan, where conventional *PKIKP–PKiKP* measurements indicate positive residuals of approximately +0.25 s (Fig. 6). Its corresponding ascending leg propagates through the IC beneath western Africa, where classic phases show negative perturbations of about −0.30 s. These regional values, inferred from the conventional single-leg data set, sum to a value consistent with the total differential time measured for the multileg phase pair. This comparison demonstrates the consistency between the newly identified multileg observations and the regional residual patterns independently established by conventional phases.

Other examples include the 12 October 2002 west Brazil event recorded at station SPA, which exhibits a mirrored geometry with a total delay of −0.60 s, combining a descending path beneath eastern North America (−0.70 s) and an ascending leg beneath southwestern Australia (0.20 s). Similar explanations apply to recordings from Antarctic station CASE of the 22 October 2002 Fiji event (Table S2), with a descending leg beneath the north Pacific and North America (−0.20 s) and an ascending leg beneath western Africa (−0.48 s). The 25 July 2004 southern Sumatra earthquake, observed at 25 European stations, produced a total delay of −0.80 ± 0.30 s in classic phase pairs, consistent with a descending leg beneath Australia–New Zealand (∼0 s) and an ascending leg beneath the northeast coast of South America (∼ −0.80 s), a region previously lacking robust coverage. Finally, the 15 June 2023 south Fiji event, recorded across North America, yielded relatively small residuals (−0.20 s), consistent with cumulative contributions from western Australia (0.20 s) and the north Atlantic (−0.40 s), both of which are sparsely sampled by classical phases (Fig. 6). This correspondence both validates the exotic-phase measurement and demonstrates its ability to extend tomography sensitivity into previously underconstrained regions.

The geometry of these observations also permits assessment of whether the residuals exhibit systematic dependence on ray direction relative to the rotation axis. As shown in Table S3, although introducing angular dependence produces a marginal reduction in the residual sum of squares, both AIC and BIC are minimized by the single-parameter isotropic model. The AIC results assign ∼62% probability to the isotropic formulation, compared with only ∼12% for the parabolic model. The lack of statistical support for higher-order angular terms, together with the geometry of *PKIKPPKIKP*, the two IC legs of which typically sample different directions relative to the rotation axis, favors the isotropic formulation.

Mantle effects and potential application in seismic tomography

It is generally assumed that mantle corrections are unnecessary for *PKIKP–PKiKP*-type phase pairs because both phases follow nearly identical mantle and outer-core paths before diverging at the IC boundary (Cao and Romanowicz, 2004; Ivan *et al.*, 2018). At the core-mantle boundary (CMB), the Fresnel zone for 1 Hz *P* waves is ∼150 km. *PKiKP–PKIKP* ray paths are ∼50 km apart and their Fresnel zones overlap, whereas *PKPbc–PKIKP* paths are ∼300 km apart, roughly twice the Fresnel zone size (Deguen, 2012). This close similarity in ray geometry minimizes the influence of mantle structure and core–mantle boundary heterogeneities on their differential travel times (Deguen, 2012; Wu and Irving, 2017).

Because *PKIKPPKIKP* and *PKiKPPKiKP* are higher-order analogs of *PKIKP* and *PKiKP*, their ray geometries through the mantle and outer core are also nearly identical. Nevertheless, to quantitatively evaluate any residual mantle influence on the *PKIKPPKIKP–PKiKPPKiKP* differential times, we computed theoretical travel-time perturbations using three global mantle models: LLNL-G3Dv (Simmons *et al.*, 2012), v3DP (Zhao, 2004), and SB4L18 (Masters *et al.*, 2000) The predicted mantle contributions are consistently small (<0.2 s), comparable to the observational uncertainty. Consequently, our *PKIKPPKIKP–PKiKPPKiKP* data set is corrected only with respect to the AK135 reference model.

Mantle effects may become significant for other phase pairs such as *PKIKPPKIKP–PKPbcPKPbc* or *PKIKPPKIKP–PKPabPKPab*, where the separation of their CMB piercing points can exceed several hundred kilometers, increasing sensitivity to lowermost-mantle heterogeneity or ultra-low velocity zones (Bréger, Tkalcic, *et al.*, 2000; Frost and Romanowicz, 2017). However, the consistency between the *PKIKPPKIKP–PKPbcPKPbc* differential times and those of *PKIKPPKIKP–*

Downloaded from pubs.geoscienceworld.org/ssa/srl/article-pdf/doi/10.1785/0220260014/8427141/srl-2026014.1.pdf by Southern University of Science and Technology of China user on 28 October 2026

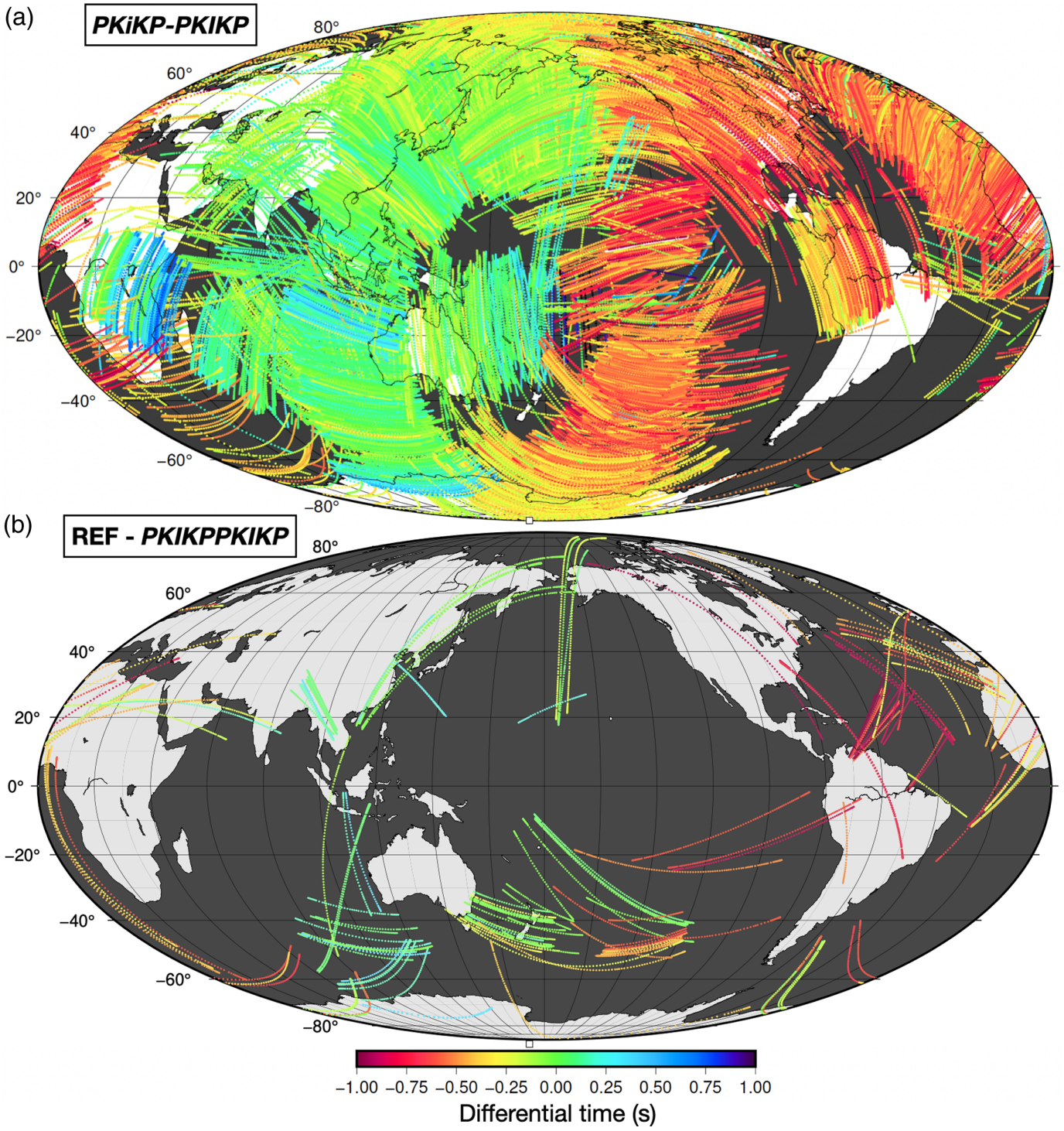

Figure 6. Ray paths of seismic phases through the Earth's IC, colored by differential delay times relative to synthetic phase pairs. (a) *PKiKP–PKIKP* (observed–computed) observations from 958 events (updated from Ivan *et al.*, 2018). Colored lines denote *PKIKP* paths in the IC. (b) *PKiKPPKiKP* (or *PKPbcPKPbc*)—*PKIKPPKIKP* (observed–computed) delay times. For visualization, ray segments are highlighted according to overlap with regions sampled by the *PKiKP–PKIKP* data set where available. The reference (REF) phase is *PKiKPPKiKP* or *PKPbcPKPbc*, depending on epicentral distance. The strong similarity between (a) and (b), despite no mantle corrections applied to (b), suggests little to no seismic anisotropy or depth-dependent *P*-wave velocity variation in the uppermost IC. The color version of this figure is available only in the electronic edition.

Downloaded from pubs.geoscienceworld.org/ssa/srl/article-pdf/doi/10.1785/0220260014/8427141/srl-2026014.1.pdf by Southern University of Science and Technology of China user on 28 October 2026

PKiKPPKiKP indicates that the observed variations can be reasonably explained without applying explicit mantle corrections.

Discussion

We successfully detect and extract information from *PKIKPPKIKP* and *PKiKPPKiKP*, multipath IC seismic phases, representing a previously untapped resource for imaging Earth's IC. Detection of such multileg phases has received limited attention due to their subtle amplitudes, the need for high SNR, and long-duration seismic records. Recent studies have suggested the utility of *PKIKP* reverberations to probe IC anisotropy and fine-scale structure, typically by comparing *PKIKPPKIKP* to outer-core references such as *PKPbcPKPbc* or *PKPabPKPab* (Bréger, Romanowicz, *et al.*, 2000; Rost and Garnero, 2004; Frost and Romanowicz, 2017; Phạm and Tkalčić, 2023). However, none have systematically analyzed the *PKiKPPKiKP* phase, which has the closest trajectory to *PKIKPPKIKP* and is thus the least affected by mantle structure when paired. Our study is the first to jointly examine this phase pair by targeting deep and intermediate-depth earthquakes with simple source time functions and strong downward energy radiation, minimizing contamination from surface reflections or complex rupture effects. Careful validation through cross correlation with synthetic waveforms, accounting for each earthquake's source mechanism, is essential for confidently identifying and interpreting these weak yet highly informative arrivals.

These multilegged phases offer two important advantages for IC studies. First, they sample regions of the IC that are sparsely covered by classical seismic phases, helping to fill blind spots in existing models, such as beneath the central Atlantic and parts of the southern hemisphere (e.g., beneath New Zealand, southeast Pacific Ocean, and south Atlantic), that lack dense ray coverage (Fig. 6). They thus provide a promising complement to standard *PKP*-family phases by retracing similar or overlapping trajectories while introducing additional sensitivity to path-averaged velocity variations and anisotropy. Second, they provide access to areas at quasi-polar angles relative to Earth's spin axis, directions typically undersampled by conventional, predominantly quasi-equatorial phases. Multidirectional sampling is critical for resolving IC anisotropy, a key property linked to asymmetric growth (Frost *et al.*, 2021). An inherent limitation is the cumulative nature of the observed delays, as the phases traverse opposite sides of the IC during descent and ascent. Decoupling the contributions from each leg remains challenging, but overlap with *PKIKP–PKiKP* differential times can help estimate the accumulated delay from the complementary leg.

Although our aim here is not to resolve anisotropy or stratification, we evaluated a potential angular dependence of the travel-time residuals relative to polar angle using a planar fitting method. Adding high-degree angular parameters resulted in statistical overfitting. The geometric complexity of the *PKIKPPKIKP* phase-whose two-core transiting legs sampling usually distinct polar angles—renders classical 1D anisotropy formulations highly undetermined. Given this geometric trade-off coupled with lower-mantle structural uncertainties and recent mineral physics constraints favoring isotropic iron phases (Belonoshko *et al.*, 2008; He *et al.*, 2022; Zhang, Wang, *et al.*, 2023), we focused our analysis mostly on the robust isotropic component.

The first-order observations presented here are consistent with previously reported IC heterogeneities (Ibourichene and Romanowicz, 2018; Ivan *et al.*, 2018; Burdick *et al.*, 2019). The spatial distribution of the interpreted time differences aligns with major patterns reported in prior studies, including the hemispherical dichotomy (Niu and Wen, 2001; Tanaka, 2012; Burdick *et al.*, 2019). Geodynamically, the east–west velocity contrasts revealed by multilegged phases (Fig. 6) echo long-standing interpretations of hemispherical asymmetry in IC growth or crystallization (Monnereau *et al.*, 2010; Cormier and Attanayake, 2013). Observed isotropic features are consistent with spherically averaged signatures of these processes, such as variations in freezing rates, crystallographic alignment (Deuss, 2014), compositional stratification (Zhang, Ni, *et al.*, 2023), IC convection (Tkalčić *et al.*, 2024), translation (Alboussière *et al.*, 2010), or superrotation (Waszek *et al.*, 2011). Our study does not directly test these geodynamic interpretations, but the compatibility of the multilegged phase observations with previously reported large-scale features adds independent support for the robustness of these anomalies.

Ultimately, this new set of multilegged phases can be extended and can be incorporated in tomography models that accommodate anisotropic terms, adaptive parameterizations, or more computationally intensive approaches, offering an immediate path forward: by exploiting a new phase family, we are extending the toolset for IC seismology. For each event, the paths of the descending and ascending segments of the *PKIKPPKIKP–PKiKPPKiKP* phase pair can be traced through these parameter cells, and the contribution of each segment to travel-time differences can be inserted into the forward matrix of an inversion, alongside conventional single-leg phases such as *PKIKP–PKiKP*. This framework naturally accounts for the combined sampling of the two legs and allows the new multileg phases to complement existing data sets. Future work can build on this foundation using amplitude-ratio attenuation (Ivan *et al.*, 2022), anisotropic (Lythgoe *et al.*, 2014; Helffrich and Mainprice, 2019; Tkalčić *et al.*, 2023), or layered frameworks (Brett *et al.*, 2022) with broader data mining to further exploit these underused phases.

Conclusions

We present the first systematic detection and use of *PKIKPPKIKP* and *PKiKPPKiKP* phase pairs at epicentral distances near 90°, identified through full-waveform synthetics matched to deep and intermediate-depth earthquakes with simple source time functions. In addition to these phases, we identify a complementary data set of *PKIKPPKIKP* versus

Downloaded from pubs.geoscienceworld.org/ssa/srl/article-pdf/doi/10.1785/0220260014/8427141/srl-2026014.1.pdf by Southern University of Science and Technology of China user on 28 October 2026

PKPbcPKPbc arrivals in the ~50° to 65° epicentral distance range. These multileg IC phases provide enhanced directional coverage, including previous blind spots such as South America or other poorly sampled regions.

We then demonstrate how their differential times can be measured via cross correlation. The time residual between observed differential times and those obtained from synthetic seismograms filtered at 0.7–2 Hz that account for earthquake source properties can be physically linked to *P*-wave velocity variations in the uppermost IC. The angular dependence analysis further indicates that the anisotropic contribution is statistically indistinguishable from zero, suggesting that global cylindrical anisotropy is not the primary driver of the observed travel-time residuals in these *PKIKPPKIKP* observations. Instead, the first-order variations are robustly captured by their isotropic component.

This study establishes a robust framework for detecting these multileg phase pairs, measuring their differential arrival times against realistic synthetic waveforms. These phase pairs provide an untapped resource with a good potential for being integrated into seismic imaging, offering a baseline for future seismic models of the IC.

Data and Resources

Seismic waveform data were obtained from the EarthScope Data Services (https://ds.iris.edu/ds/nodes/dmc/data/) and the European Integrated Data Archive (EIDA, https://www.orfeus-eu.org/data/). Earthquake source parameters, including moment tensors and source duration estimates, were sourced from the Global Centroid Moment Tensor (Global CMT) catalog (https://www.globalcmt.org/). Phase picks, including occasional reports of multipath core phases, were cross referenced from the International Seismological Centre (ISC) Bulletin (https://www.isc.ac.uk/iscbulletin/search/bulletin/). Synthetic seismograms were generated using the QSSP code (Wang *et al.*, 2017), which accounts for a spherical, self-gravitating Earth with atmosphere, ocean, mantle, and core structure. Ray-path computations and travel-time predictions were performed using the TauP Toolkit (Crotwell *et al.*, 1999). All map and figure visualizations were produced with Generic Mapping Tools (GMT) version 6 (Wessel *et al.*, 2019). All websites were last accessed in August 2026. All results generated within this study are available in the supplemental material.

Declaration of Competing Interests

The authors acknowledge that there are no conflicts of interest recorded.

Acknowledgments

X. H. acknowledges financial support from the National Natural Science Foundation of China (Grant Number 42276049). L. P. is supported by the Romanian Ministry of Education and Research, through the NUCLEU SOL4RISC Project Number PN23360201. The authors are grateful to Barbara Romanowicz, Olga Usoltseva, Vernon Cormier, Vladimir Ovtchinnikov, and Satoru Tanaka for their insightful feedback during the preparation of this article. The authors also thank four anonymous reviewers for constructive comments that improved this article.

References

Akaike, H. (1973). Information theory and an extension of the maximum likelihood principle, in *Proc. of the 2nd International Symposium on Information Theory*, B. N. Petrov and F. Csaki (Editors), Akademiai Kiado, Budapest, 267–281.

Alboussière, T., R. Deguen, and M. Melzani (2010). Melting-induced stratification above the Earth's inner core due to convective translation, *Nature* **466,** 744–747, doi: 10.1038/nature09257.

Aubert, J., H. Amit, G. Hulot, and P. Olson (2008). Thermochemical flows couple the Earth's inner core growth to mantle heterogeneity, *Nature* **454,** 758–761, doi: 10.1038/nature07109.

Belonoshko, A. B., N. V. Skorodumova, A. Rosengren, and B. Johansson (2008). Elastic anisotropy of Earth's inner core, *Science* **319,** no. 5864, 797–800, doi: 10.1126/science.1150302.

Bréger, L., B. Romanowicz, and S. Rousset (2000). New constraints on the structure of the inner core from P′P′, *Geophys. Res. Lett.* **27,** 2781–2784, doi: 10.1029/1999GL008467.

Bréger, L., H. Tkalcic, and B. A. Romanowicz (2000). The effect of D″ on PKP (AB-DF) travel time residuals and possible implications for inner core structure, *Earth Planet. Sci. Lett.* **175,** 133–143, doi: 10.1016/S0012-821X(99)00286-1.

Brett, H., and A. Deuss (2020). Inner core anisotropy measured using new ultra-polar PKIKP paths, *Geophys. J. Int.* **223,** 1230–1246, doi: 10.1093/gji/ggaa348.

Brett, H., R. Hawkins, L. Waszek, K. Lythgoe, and A. Deuss (2022). 3D transdimensional seismic tomography of the inner core, *Earth Planet. Sci. Lett.* **593,** 117688, doi: 10.1016/j.epsl.2022.117688.

Burdick, S., L. Waszek, and V. Lekić (2019). Seismic tomography of the uppermost inner core, *Earth Planet. Sci. Lett.* **528,** 115789, doi: 10.1016/j.epsl.2019.115789.

Cao, A., and B. Romanowicz (2004). Hemispherical transition of seismic attenuation at the top of the Earth's inner core, *Earth Planet. Sci. Lett.* **228,** 243–253, doi: 10.1016/j.epsl.2004.09.032.

Cormier, V. F., and J. Attanayake (2013). Earth's solid inner core: Seismic implications of freezing and melting, *J. Earth Sci.* **24,** 683–698, doi: 10.1007/s12583-013-0363-9.

Crotwell, H. P., T. J. Owens, and J. Ritsema (1999). The TauP ToolKit: Flexible seismic travel-time and ray-path utilities, *Seismol. Res. Lett.* **70,** 154–160, doi: 10.1785/gssrl.70.2.154.

Deguen, R. (2012). Structure and dynamics of Earth's inner core, *Earth Planet. Sci. Lett.* **333–334,** 211–225, doi: 10.1016/j.epsl.2012.04.038.

Deguen, R., T. Alboussiere, and P. Cardin (2013). Thermal convection in Earth's inner core with phase change at its boundary, *Geophys. J. Int.* **194,** 1310–1334, doi: 10.1093/gji/ggt202.

Deuss, A. (2014). Heterogeneity and anisotropy of Earth's inner core, *Annu. Rev. Earth Planet. Sci.* **42,** 103–126, doi: 10.1146/annurev-earth-060313-054658.

Dziewonski, A. M., T.-A. Chou, and J. H. Woodhouse (1981). Determination of earthquake source parameters from waveform data for studies of global and regional seismicity, *J. Geophys. Res. Solid Earth* **86,** 2825–2852, doi: 10.1029/JB086iB04p02825.

Ekström, G., M. Nettles, and A. M. Dziewonski (2012). The global CMT project 2004–2010: Centroid-moment tensors for 13,017 earthquakes, *Phys. Earth Planet. In.* **200–201,** 1–9, doi: 10.1016/j.pepi.2012.04.002.

Downloaded from pubs.geoscienceworld.org/ssa/srl/article-pdf/doi/10.1785/0220260014/8427141/srl-2026014.1.pdf by Southern University of Science and Technology of China user on 28 October 2026

Frost, D. A., and B. Romanowicz (2017). Constraints on inner core anisotropy using array observations of P′P′, *Geophys. Res. Lett.* **44,** 10,878–10,886, doi: 10.1002/2017GL075049.

Frost, D. A., M. Lasbleis, B. Chandler, and B. Romanowicz (2021). Dynamic history of the inner core constrained by seismic anisotropy, *Nat. Geosci.* **14,** 531–535, doi: 10.1038/s41561-021-00761-w.

Gubbins, D., B. Sreenivasan, J. Mound, and S. Rost (2011). Melting of the Earth's inner core, *Nature* **473,** 361–363, doi: 10.1038/nature10068.

He, Y., S. Sun, D. Y. Kim, B. G. Jang, H. Li, and H. K. Mao (2022). Superionic iron alloys and their seismic velocities in Earth's inner core, *Nature* **602,** no. 7896, 258–262, doi: 10.1038/s41586-021-04361-x.

Helffrich, G., and D. Mainprice (2019). Anisotropy at the inner core boundary, *Geophys. Res. Lett.* **46,** 11,959–11,967, doi: 10.1029/2019GL083644.

Ibourichene, A., and B. Romanowicz (2018). Detection of small scale heterogeneities at the inner core boundary, *Phys. Earth Planet. In.* **281,** 55–67, doi: 10.1016/j.pepi.2018.03.003.

Irving, J. C. E., and A. Deuss (2011). Hemispherical structure in inner core velocity anisotropy, *J. Geophys. Res. Solid Earth* **116,** no. B4, doi: 10.1029/2010JB007942.

Ivan, M., and X. He (2017). Uppermost inner core heterogeneity from differential travel times of PKIKP vs. PKP-Bdiff and PKP-Cdiff phases, *Pure Appl. Geophys.* **174,** no. 1, 249–259, doi: 10.1007/s00024-016-1391-z.

Ivan, M., L. Petrescu, and R. Wang (2022). An attenuating, isotropic and heterogeneous uppermost inner core: Evidence from global PKiKP-PKIKP amplitude ratio tomography, *Geophys. J. Int.* **231,** 159–171, doi: 10.1093/gji/ggac142.

Ivan, M., R. Wang, and R. Hofstetter (2018). Non quasi-hemispherical seismological pattern of the earth's uppermost inner core, *Sci. Rep.* **8,** 2270, doi: 10.1038/s41598-018-20657-x.

Kay, S. M. (1993). *Fundamentals of Statistical Signal Processing, Volume I, Estimation Theory*, Prentice Hall, Englewood Cliffs, New Jersey.

Kennett, B. L., E. R. Engdahl, and R. Buland (1995). Constraints on seismic velocities in the Earth from traveltimes, *Geophys. J. Int.* **122,** 108–124, doi: 10.1111/j.1365-246X.1995.tb03540.x.

Landeau, M., J. Aubert, and P. Olson (2017). The signature of inner-core nucleation on the geodynamo, *Earth Planet. Sci. Lett.* **465,** 193–204, doi: 10.1016/j.epsl.2017.02.004.

Lentas, K., D. Di Giacomo, J. Harris, and D. A. Storchak (2019). The ISC Bulletin as a comprehensive source of earthquake source mechanisms, *Earth Syst. Sci. Data* **11,** 565–578, doi: 10.5194/essd-11-565-2019.

Lythgoe, K. H., A. Deuss, J. F. Rudge, and J. A. Neufeld (2014). Earth's inner core: Innermost inner core or hemispherical variations? *Earth Planet. Sci. Lett.* **385,** 181–189, doi: 10.1016/j.epsl.2013.10.049.

Masters, G., G. Laske, H. Bolton, and A. Dziewonski (2000). The relative behavior of shear velocity, bulk sound speed, and compressional velocity in the Mantle: Implications for chemical and thermal structure, in *Earth's Deep Interior*, S. Karato, A. M. Forte, R. C. Liebermann, G. Masters, and L. Stixrude (Editors), AGU Monograph, Vol. 117, American Geophysical Union, Washington, DC.

Monnereau, M., M. Calvet, L. Margerin, and A. Souriau (2010). Lopsided growth of Earth's inner core, *Science* **328,** 1014–1017, doi: 10.1126/science.1186212.

Niu, F., and L. Wen (2001). Hemispherical variations in the seismic velocity at the top of the Earth's inner core, *Nature* **410,** 1081–1084, doi: 10.1038/35074073.

Phạm, T. S., and H. Tkalčić (2023). Up-to-fivefold reverberating waves through the Earth's center and distinctly anisotropic innermost inner core, *Nat. Commun.* **14,** 754, doi: 10.1038/s41467-023-36074-2.

Rost, S., and E. J. Garnero (2004). A study of the uppermost inner core from PKKP and P′P′ differential traveltimes, *Geophys. J. Int.* **156,** 565–574, doi: 10.1111/j.1365-246X.2004.02139.x.

Schwarz, G. (1978). Estimating the dimension of a model, *Ann. Stat.* **6,** no. 2, 461–464, doi: 10.1214/aos/1176344136.

Simmons, N. A., S. C. Myers, G. Johannesson, and E. Matzel (2012). LLNL-G3Dv3: Global P wave tomography model for improved regional and teleseismic travel time prediction, *J. Geophys. Res. Solid Earth* **117,** no. B10, doi: 10.1029/2012JB009525.

Stroujkova, A., and V. F. Cormier (2004). Regional variations in the uppermost 100 km of the Earth's inner core, *J. Geophys. Res. Solid Earth* **109,** 1–12, doi: 10.1029/2004JB002976.

Tanaka, S. (2012). Depth extent of hemispherical inner core from PKP (DF) and PKP (Cdiff) for equatorial paths, *Phys. Earth Planet. In.* **210,** 50–62, doi: 10.1016/j.pepi.2012.08.001.

Tanaka, S., and H. Hamaguchi (1997). Degree one heterogeneity and hemispherical variation of anisotropy in the inner core from PKP (BC)–PKP(DF) times, *J. Geophys. Res. Solid Earth* **102,** 2925–2938, doi: 10.1029/96JB03187.

Tkalčić, H. (2015). Complex inner core of the Earth: The last frontier of global seismology, *Rev. Geophys.* **53,** 59–94, doi: 10.1002/2014RG000469.

Tkalčić, H., A. B. Belonoshko, J. B. Muir, M. Mattesini, L. Moresi, and L. Waszek (2024). Imaging the top of the Earth's inner core: A present-day flow model, *Sci. Rep.* **14,** 8999, doi: 10.1038/s41598-024-59520-7.

Tkalčić, H., T. P. Costa de Lima, T. S. Phạm, and S. Tanaka (2023). Inner core anisotropy from antipodal PKIKP traveltimes, in *Core-Mantle Co-Evolution: An Interdisciplinary Approach*, 165–189, doi: 10.1002/9781119526919.ch10.

Wang, R., S. Heimann, Y. Zhang, H. Wang, and T. Dahm (2017). Complete synthetic seismograms based on a spherical self-gravitating Earth model with an atmosphere–ocean–mantle–core structure, *Geophys. J. Int.* **210,** 1739–1764, doi: 10.1093/gji/ggx259.

Waszek, L., and A. Deuss (2011). Distinct layering in the hemispherical seismic velocity structure of Earth's upper inner core, *J. Geophys. Res. Solid Earth* **116,** no. B12, doi: 10.1029/2011JB008650.

Waszek, L., J. Irving, and A. Deuss (2011). Reconciling the hemispherical structure of Earth's inner core with its super-rotation, *Nat. Geosci.* **4,** 264–267, doi: 10.1038/ngeo1083.

Wessel, P., J. F. Luis, L. Uieda, R. Scharroo, F. Wobbe, W. H. F. Smith, and D. Tian (2019). The Generic Mapping Tools version 6, *Geochem. Geophys. Geosyst.* **20,** 5556–5564, doi: 10.1029/2019GC008515.

Downloaded from pubs.geoscienceworld.org/ssa/srl/article-pdf/doi/10.1785/0220260014/8427141/srl-2026014.1.pdf by Southern University of Science and Technology of China user on 28 October 2026

Wu, W., and J. C. Irving (2017). Using PKiKP coda to study heterogeneity in the top layer of the inner core's western hemisphere, *Geophys. J. Int.* **209,** 672–687, doi: 10.1093/gji/ggx047.

Young, M. K., H. Tkalcić, T. Bodin, and M. Sambridge (2013). Global P wave tomography of Earth's lowermost mantle from partition modeling, *J. Geophys. Res.: Solid Earth*, **118,** no. 10, 5467–5486, doi: 10.1002/jgrb.50391.

Zhang, B., S. Ni, W. Wu, Z. Shen, W. Wang, D. Sun, and Z. Wu (2023). Small-scale layered structures at the inner core boundary, *Nat. Commun.* **14,** 6362, doi: 10.1038/s41467-023-42177-7.

Zhang, Y., Y. Wang, Y. Huang, J. Wang, Z. Liang, L. Hao, Z. Gao, J. Li, Q. Wu, H. Zhang, *et al.* (2023). Collective motion in hcp-Fe at Earth's inner core conditions, *Proc. Natl. Acad. Sci.* **120,** no. 41, e2309952120, doi: 10.1073/pnas.2309952120.

Zhao, D. (2004). Global tomographic images of mantle plumes and subducting slabs: Insight into deep Earth dynamics. *Phys. Earth Planet. In.* **146,** 3–34, doi: 10.1016/j.pepi.2003.07.032.

Manuscript received 12 January 2026
Published online 27 October 2026

Downloaded from pubs.geoscienceworld.org/ssa/srl/article-pdf/doi/10.1785/0220260014/8427141/srl-2026014.1.pdf by Southern University of Science and Technology of China user on 28 October 2026